ACADEMIC PRESS

Available online at www.sciencedirect.com

SCIENCE DIRECT®

Journal of Computational Physics 184 (2003) 149–162

JOURNAL OF COMPUTATIONAL PHYSICS

www.elsevier.com/locate/jcp

Spectral elements and field separation for an acoustic fluid subject to cavitation

Michael A. Sprague*, Thomas L. Geers

Department of Mechanical Engineering, University of Colorado at Boulder, Boulder, CO 80309-0427 USA

Received 26 September 2001; received in revised form 18 September 2002; accepted 2 October 2002

Abstract

Spectral elements based on Legendre polynomials are used to improve an existing finite-element method for simulating a highly nonlinear field phenomenon: fluid cavitation in an underwater-shock environment. Further improvement is provided by separation of the total field into its equilibrium, incident, and scattered components. These enhancements promise to make the finite-element method suitable for practical, three-dimensional engineering computations.

Keywords: Fluid–structure interaction; Underwater shock; Wave propagation

1. Introduction

In this paper we examine the effectiveness of two techniques when applied to the computational simulation of fluid cavitation as it arises in the problem of a ship excited by an underwater-shock wave. The first technique is the use of spectral elements to discretize the fluid domain [12,21,22,24]. The second technique is separation of the total fluid field into known and unknown fields [15].

1.1. Cavitation

In the context of underwater shock, cavitation, i.e., boiling, occurs as a result of the reflection of the shock wave from the free surface and/or wetted structure, which causes the pressure in the water to fall below its vapor pressure [1,11]. The instantaneous bulk modulus of cavitated water is orders of magnitude smaller than that of uncavitated water, which is the crux of the nonlinearity. A simple but satisfactory constitutive model is a bilinear one, in which the bulk modulus is that of water as an acoustic medium when the condensation (negative volume strain) is positive, and zero when the condensation is negative [1].

* Corresponding author.
E-mail address: Michael.Sprague@Colorado.edu (M.A. Sprague).

0021-9991/02/$ - see front matter
PII: S0021-9991(02)00024-4

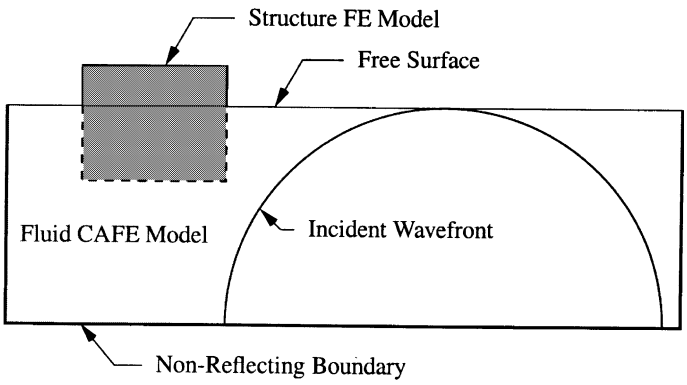

Fig. 1. CAFE approach for ship-shock calculations; incident wavefront shown just before the onset of cavitation.

Although pure water has been found to sustain substantial negative pressures, even small amounts of dissolved gases nullify the effect [6].

In 1984, Felippa and DeRuntz [7] developed a cavitating acoustic finite element (CAFE) based on the work of Newton [17–20] in which the wave field in the fluid is represented by a scalar displacement potential. Spatial discretization was performed with trilinear, isoparametric, eight-node brick elements, and the CAFE dynamical equations were integrated in time with a central-difference algorithm. Numerical damping was employed to suppress the occurrence of spurious cavitation, which they called *frothing*. A six-node wedge element was added later [8].

The CAFE solution strategy for a ship-shock simulation consists of four steps (Fig. 1): (1) construct a finite-element (FE) model of the structure, (2) interface it with a CAFE model of the water region in which cavitation is expected to occur, (3) enclose the CAFE mesh with a non-reflecting computational boundary, and (4) start integrating the CAFE equations just before the incident wavefront reaches either the free surface or the structure [7,25]. Unfortunately, because of high mesh dispersion, extremely refined CAFE meshes are required to obtain accurate structural responses [26,28]. Hence, CAFE computation constitutes an unacceptable overhead burden, given that the structure is the focus of interest.

Seeking to reduce CAFE overhead in two-dimensional simulations, van Aanhold et al. [31] dramatically truncated the mesh in the horizontal directions with considerable success. In addition, Sprague and Geers [28] used one-dimensional models to show that the CAFE mesh may also be truncated from below, provided that the mesh covers all regions that exhibit *fluid accretion*, the presence of an uncavitated layer of water that separates the structure from a cavitated layer. However, even with mesh truncation, current CAFE simulation is simply too resource intensive for three-dimensional engineering computations.

1.2. Improvement of CAFE simulation

As mentioned above, we consider two techniques for improving CAFE simulation:

- discretization with high-order spectral elements based on Legendre polynomials,
- separation of the total field into equilibrium, incident, and scattered fields.

We evaluate these techniques with a benchmark model consisting of a semi-infinite, one-dimensional unit-area fluid column that supports a 2-degree-of-freedom (2-DOF) mass-spring oscillator; the lower mass represents the ship's hull and the upper mass its internal structure and equipment. This model was productively employed in a recent evaluation of CAFE and wet-surface-approximation methods [28]. The benchmark solutions are the product of a super-refined CAFE model.

The effectiveness of each technique is evaluated with the *comprehensive error factor* [10,27], given by $C = \sqrt{M^2 + P^2}$, in which $M = \sqrt{\vartheta_{cc}/\vartheta_{bb}} - 1$ and $P = 1 - \vartheta_{cb}/\sqrt{\vartheta_{cc}\vartheta_{bb}}$, where

$$\vartheta_{cc} = (t_2 - t_1)^{-1} \int_{t_1}^{t_2} c^2(t)\,\mathrm{d}t, \quad \vartheta_{bb} = (t_2 - t_1)^{-1} \int_{t_1}^{t_2} b^2(t)\,\mathrm{d}t, \quad \vartheta_{cb} = (t_2 - t_1)^{-1} \int_{t_1}^{t_2} c(t)b(t)\,\mathrm{d}t. \tag{1}$$

In these equations, $c(t)$ is a candidate solution in the form of a response history, $b(t)$ is the corresponding benchmark history, and $t_1 \leqslant t \leqslant t_2$ is the time span of interest. M is the *magnitude error factor*, which is insensitive to phase discrepancies, and P is the *phase error factor*, which is insensitive to magnitude discrepancies.

2. Cavitating acoustic spectral elements

It is well known that low-order finite elements exhibit high numerical dispersion when applied to wave-propagation problems [14]. High-order elements generate less dispersion, but typically exhibit small spurious oscillations; however, the reduced dispersion more than compensates for the presence of the oscillations [16]. The most effective of the high-order finite elements appear to be spectral elements, which display impressive wave-propagation capabilities [5,12,21,22,24]. Further, spectral elements are well suited to parallel implementation [9].

2.1. Governing equations

We seek to construct cavitating acoustic spectral elements (CASE) based on the irrotational-motion formulation of Newton [17–20], which employs two scalar variables: dynamic condensation $s(\vec{X}, t)$ and displacement potential $\psi(\vec{X}, t)$, where $\vec{X}$ is the global-position vector of a fluid material point. These variables are related as

$$s = \nabla^2\psi, \quad \ddot{\psi} = \begin{cases} c^2 s, & c^2 s > -p_{\mathrm{E}}, \\ -p_{\mathrm{E}}, & c^2 s \leqslant -p_{\mathrm{E}}, \end{cases} \tag{2}$$

where p_{E} is the equilibrium pressure, i.e., the sum of the atmospheric pressure p_{atm} and the hydrostatic pressure $p_{\mathrm{hyd}}(\vec{X})$, c is the sound speed in water, and an overdot denotes a temporal derivative. The water vapor pressure is so much smaller than the large dynamic pressures involved that it has been taken as zero.

Total fluid pressure and displacement may be obtained as $p = \ddot{\psi} + p_{\mathrm{E}}$ and $\vec{u} = -\rho^{-1}\vec{\nabla}\psi + \vec{u}_{\mathrm{E}}$, where ρ is the initial fluid density (a constant), and $\vec{u}_{\mathrm{E}}$ is the static displacement field produced by p_{E}. The use of scalar field quantities, as opposed to vector quantities, minimizes the number of unknowns at each point in the fluid domain and enforces irrotationality of the flow.

2.2. Discretization

A subparametric discretization is used; first-order basis functions are used for geometry representation and higher-order basis functions are used for field-variable representation. The fluid volume Ω is separated into n_{e} hexagonal elements defined by eight corner points. The geometry within each element is expressed as

$$X = \boldsymbol{\varphi}^{\mathrm{T}}\mathbf{X}, \quad Y = \boldsymbol{\varphi}^{\mathrm{T}}\mathbf{Y}, \quad Z = \boldsymbol{\varphi}^{\mathrm{T}}\mathbf{Z}, \tag{3}$$

where $\mathbf{X}$, $\mathbf{Y}$, $\mathbf{Z}$ are column vectors of element-corner-point locations in global coordinates, $\boldsymbol{\varphi}$ is a column vector of trilinear shape functions, and the T-superscript denotes vector transposition.

The dependent field variables are represented within each element as

$$s(\xi,\eta,\zeta,t) = \boldsymbol{\phi}^{\mathrm{T}}(\xi,\eta,\zeta)\mathbf{s}(t) = \sum_{i,j,k=0}^{N} \phi_i(\xi)\phi_j(\eta)\phi_k(\zeta)s_{ijk}(t),$$

$$\psi(\xi,\eta,\zeta,t) = \boldsymbol{\phi}^{\mathrm{T}}(\xi,\eta,\zeta)\boldsymbol{\psi}(t) = \sum_{i,j,k=0}^{N} \phi_i(\xi)\phi_j(\eta)\phi_k(\zeta)\psi_{ijk}(t), \tag{4}$$

where $\mathbf{s}$ and $\boldsymbol{\psi}$ are column vectors of $(N+1)^3$ time-dependent nodal values (s_{ijk} and ψ_{ijk}), and $\boldsymbol{\phi}$ is a column vector composed of one dimension, Nth-order-polynomial basis functions $\phi_i(\xi)\phi_j(\eta)\phi_k(\zeta)$; ξ, η, and ζ are element natural coordinates $(-1 \leqslant \xi,\eta,\zeta \leqslant 1)$.

The essence of the spectral-element method lies in the choice of ϕ; here, we use Lagrangian interpolants given by [23]

$$\phi_i(\xi) = -\frac{(1-\xi^2)P'_N(\xi)}{N(N+1)P_N(\xi_i)(\xi-\xi_i)}, \tag{5}$$

where P_N is the Legendre polynomial of degree N, the prime denotes differentiation with respect to argument, and ξ_i is the ith Gauss–Lobatto–Legendre (GLL) quadrature point defined by the corresponding root of

$$(1-\xi^2)P'_N(\xi) = 0. \tag{6}$$

The expression (5) satisfies the relation

$$\phi_i(\xi_j) = \delta_{ij}, \tag{7}$$

where δ_{ij} is the Kronecker delta. The one-dimensional Lagrangian interpolants (5) are shown in Fig. 2 for $N = 1$, 4, 8, and 16. Element–node locations are coincident with the quadrature points, which are located at the $(N+1)$ zeros of (6).

The governing equations (2a) are discretized with a standard Galerkin approach [32]: premultiplication of (2a) by $\boldsymbol{\phi}$, integration over the fluid volume, and application of Green's first identity. This yields

$$\int_\Omega \boldsymbol{\phi} s \,\mathrm{d}\Omega + \int_\Omega \vec{\nabla}\boldsymbol{\phi}\cdot\vec{\nabla}\psi \,\mathrm{d}\Omega = \int_\Gamma \boldsymbol{\phi}\vec{\nabla}\psi\cdot\vec{\boldsymbol{n}}\,\mathrm{d}\Gamma, \tag{8}$$

where Γ is the surface of the fluid volume, and $\vec{\boldsymbol{n}}$ is the outward-normal vector to Γ. Substitution of (4) into the dependent variables on the left-hand side of (8) yields the algebraic equations

$$\mathbf{Q}\mathbf{s} + \mathbf{H}\boldsymbol{\psi} = \mathbf{b}, \tag{9}$$

where the capacitance matrix, reactance matrix, and boundary-interaction vector are given by

$$\mathbf{Q} = \int_\Omega \boldsymbol{\phi}\boldsymbol{\phi}^{\mathrm{T}}\,\mathrm{d}\Omega, \quad \mathbf{H} = \int_\Omega \vec{\nabla}\boldsymbol{\phi}\cdot\vec{\nabla}\boldsymbol{\phi}^{\mathrm{T}}\,\mathrm{d}\Omega, \quad \mathbf{b} = \int_\Gamma \boldsymbol{\phi}\vec{\nabla}\psi\cdot\vec{\boldsymbol{n}}\,\mathrm{d}\Gamma, \tag{10}$$

respectively. Note that in $\mathbf{b}$, $\vec{\nabla}\psi$ is maintained in its continuum form because it is provided by the displacements at the non-reflecting and structure–fluid boundaries.

The integrals in (10) are approximated with GLL quadrature. Because nodes and quadrature points are coincident, and because of (7), $\mathbf{Q}$ is diagonal, which facilitates the use of the explicit integration scheme used here. In (9), the matrix-vector product $\mathbf{H}\boldsymbol{\psi}$ may be evaluated at the element level without explicitly

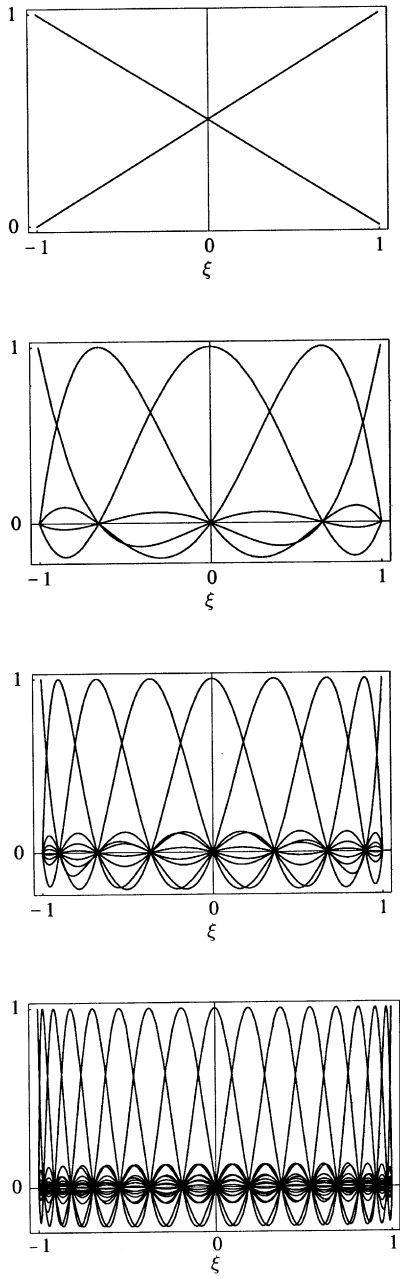

Fig. 2. One-dimensional Lagrangian interpolants based on Legendre polynomials for $N = 1$, 4, 8, and 16.

forming **H**. Indeed, for three-dimensional implementation, the most efficient evaluation of the matrix-vector product is achieved at the element level with *tensor-product factorization* [13], which offers significant savings in required operations and memory storage. However, for the simple one-dimensional elements used here, the element matrices are assembled into a global band-diagonal matrix.

The bilinear constitutive equations (2b), when evaluated at each node, become

$$\{\ddot{\boldsymbol{\psi}}\}_j = \begin{cases} \{c^2\mathbf{s}\}_j, & \{c^2\mathbf{s}\}_j > -\{\mathbf{p}_\mathrm{E}\}_j, \\ -\{\mathbf{p}_\mathrm{E}\}_j, & \{c^2\mathbf{s}\}_j \leqslant -\{\mathbf{p}_\mathrm{E}\}_j, \end{cases} \tag{11}$$

where $\mathbf{p}_\mathrm{E}$ is a column vector of nodal equilibrium pressures.

As in [7], (11) are discretized in time with a conditionally stable central-difference algorithm and are integrated with a constant time increment Δt. Numerical damping proportional to $\dot{s}$ is again used to suppress frothing. As seen in Fig. 2, the CASE-node locations are clustered near the element endpoints. Because of this, an Nth-order spectral element produces a smaller Courant–Friedrichs–Lewy (CFL) stability limit [4] than an Nth-order finite element of equal size with uniform node spacing. Finally, the fluid equations must be initialized with the incident-wave properties.

3. Field separation

The far field produced by an acoustic-shock wave in an unbounded fluid (the incident field) is relatively easy to define. Hence, in order to minimize the propagation of a known discontinuous wave through the CAFE mesh, integration of the CAFE dynamical equations is best begun just prior to the impingement of the incident wavefront on either the free surface or the structure [7]. Fig. 1 shows a common geometry in which the incident wavefront has reached the free surface but is still far from the structure, so the incident wave must still be propagated through a substantial portion of the mesh before it reaches the structure. The situation is easily reversed by a simple alteration of the geometry.

In order to avoid propagating the incident wave through the mesh, we employ a technique used frequently in linear scattering problems, which consists of separating the total field into a known incident field and an unknown scattered field [15]. The technique was applied to FE calculations by Chan [2,3], who used his mesh for scattered-field calculations only. Further, it has been applied to finite-difference time-domain linear electrodynamics calculations [30]. Field separation may also be used for nonlinear scattering problems, with or without boundaries.

3.1. Governing equations

Here, we separate the total field into three component fields: equilibrium, incident, and scattered. The equilibrium field is easily determined as that due to atmospheric plus hydrostatic pressure, the incident field is readily determined as that due to an acoustic-shock wave propagating in a homogeneous, unbounded fluid, and the scattered field is caused by the presence of both the structure and the free surface. Hence, we write $s = s_\mathrm{I} + s_\mathrm{S}$ and $\psi = \psi_\mathrm{I} + \psi_\mathrm{S}$, where all of the variables constitute deviations from equilibrium.

Because the incident field is cavitation free, we write from (2)

$$s_\mathrm{I} = \nabla^2\psi_\mathrm{I}, \quad \ddot{\psi}_\mathrm{I} = c^2 s_\mathrm{I}. \tag{12}$$

Notice that (12) is easily reduced to the acoustic wave equation. Introducing $s = s_\mathrm{I} + s_\mathrm{S}$ and $\psi = \psi_\mathrm{I} + \psi_\mathrm{S}$ into (2) and employing (12), we obtain

$$s_\mathrm{S} = \nabla^2\psi_\mathrm{S}, \quad \ddot{\psi}_\mathrm{S} = \begin{cases} c^2 s_\mathrm{S}, & c^2 s_\mathrm{S} > -(p_\mathrm{E} + p_\mathrm{I}), \\ -(p_\mathrm{E} + p_\mathrm{I}), & c^2 s_\mathrm{S} \leqslant -(p_\mathrm{E} + p_\mathrm{I}), \end{cases} \tag{13}$$

where $p_\mathrm{I} = \ddot{\psi}_\mathrm{I}$ is the incident pressure. Note that the second of (13) involves a dynamic quantity on the right-hand sides of the inequalities, in contrast to the second of (2). In addition, the free-surface (FS) essential boundary condition for the scattered-field equations is *time dependent*, i.e.,

$$p_\mathrm{S}\big|_\mathrm{FS} + p_\mathrm{I}\big|_\mathrm{FS} = 0. \tag{14}$$

3.2. Discretization

We spatially discretize (13a) with a standard Galerkin approach as described in Section 2.2; the resulting separated-field CASE equations are

$$\mathbf{Q}\mathbf{s}_{\mathrm{S}} + \mathbf{H}\boldsymbol{\psi}_{\mathrm{S}} = \mathbf{b}_{\mathrm{S}},$$

$$\{\ddot{\boldsymbol{\psi}}_{\mathrm{S}}\}_j = \begin{cases} \{c^2\mathbf{s}_{\mathrm{S}}\}_j, & \{c^2\mathbf{s}_{\mathrm{S}}\}_j > -\{\mathbf{p}_{\mathrm{E}} + \mathbf{p}_{\mathrm{I}}\}_j, \\ -\{\mathbf{p}_{\mathrm{E}} + \mathbf{p}_{\mathrm{I}}\}_j, & \{c^2\mathbf{s}_{\mathrm{S}}\}_j \leqslant -\{\mathbf{p}_{\mathrm{E}} + \mathbf{p}_{\mathrm{I}}\}_j, \end{cases} \tag{15}$$

where $\mathbf{Q}$ and $\mathbf{H}$ are defined in (10), $\mathbf{p}_{\mathrm{I}}$ is a column vector of nodal incident pressures, and the scattered boundary-interaction vector $\mathbf{b}_{\mathrm{S}}$ is defined by

$$\mathbf{b}_{\mathrm{S}} = \int_{\Gamma} \phi \vec{\nabla}\psi_{\mathrm{S}} \cdot \vec{n}\, \mathrm{d}\Gamma. \tag{16}$$

Temporal integration is again performed following [7]. However, integration of the separated-field equations is simplified because the initial conditions for the scattered field are quiescent.

4. Evaluation

The benchmark model mentioned in Section 1.2 is shown in Fig. 3. The hull mass is m_1 and the total mass of internal structure and equipment is m_2. The displacements of m_1 and m_2 are $u_1(t)$ and $u_2(t)$, respectively. Depth relative to m_1 is denoted by X and the mesh is terminated at d_{PW} with a plane-wave (ρc-damper) boundary, which is exact for one-dimensional acoustic waves. The fluid mesh outputs dis-

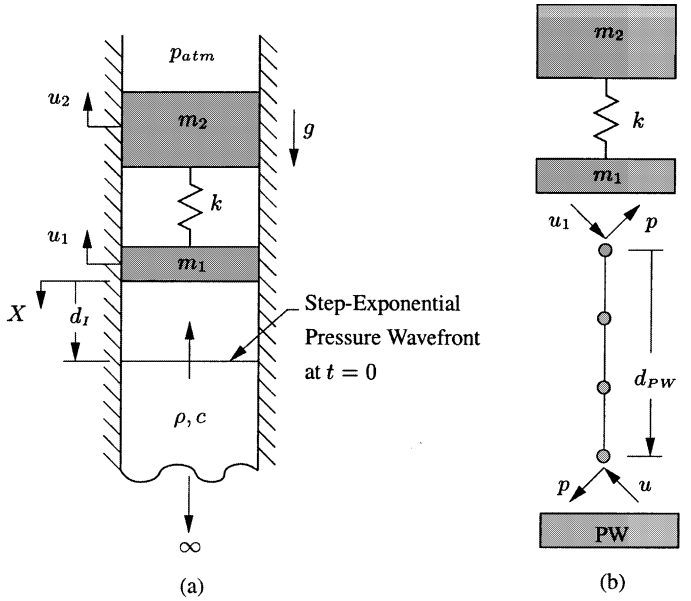

Fig. 3. Benchmark problem: (a) physical model, (b) discrete model; data transfers between components are denoted by arrows.

placement-potential (actually pressure) data at its end nodes and accepts displacement data at those nodes through the boundary-interaction vector.

The incident field driving the hull mass is a plane, upward propagating, step-exponential acoustic wave defined by

$$p_{\mathrm{I}}(X,t) = p_{\mathrm{M}} \exp\left[-\frac{t+(X-d_{\mathrm{I}})/c}{\tau}\right] \mathrm{H}[t+(X-d_{\mathrm{I}})/c], \tag{17}$$

where p_{M} and τ are the peak pressure and decay time, respectively, and $H()$ is the Heaviside step-function. At $t = 0$, the incident wavefront is located at a standoff d_{I} from m_1.

The physical properties used in all calculations are $\rho = 1025\,\mathrm{kg/m^3}$, $c = 1500\,\mathrm{m/s}$, $p_{\mathrm{atm}} = 0.101\,\mathrm{MPa}$, and $g = 9.81\,\mathrm{m/s^2}$. For the ship model, $m_2/m_1 = 5$ and $m_1 = 867\,\mathrm{kg}$, which produce an equilibrium draft for the corresponding three-dimensional structure of 5.08 m. The spring stiffness k is such that the fixed-base natural frequency of m_2 is 5 Hz. The incident wave corresponds to the shock wave generated by a 45.4 kg charge of HBX-1 at a 10.1 m standoff from the wet surface of the hull mass, so that $p_{\mathrm{M}} = 16.15$ MPa and $\tau = 0.423$ ms [29].

The benchmark results are the product of a one-dimensional CAFE research code, which has been validated [28] with the benchmark problem of Bleich and Sandler [1]. The super-refined CAFE mesh has 24,000 equal-length elements and employs a mesh with $d_{\mathrm{PW}} = 3\,\mathrm{m}$, which extends below the 2.5 m maximum depth of cavitation. In this and all other calculations, the numerical-damping froth-suppression *parameter* β is set at 0.5 [7] and the time increment is set at one half the CFL limit.

4.1. Evaluation of CASE

We first examine results generated with one-dimensional $(N+1)$-node spectral elements for the total field, i.e., without field separation. The computations begin with the incident wavefront located at the first node off of m_1, and with the pressure at the wavefront node set at $p_{\mathrm{M}}/2$ [7]. Like the benchmark model, the CASE models utilize equal-length elements and are terminated at $d_{\mathrm{PW}} = 3\,\mathrm{m}$ with the plane-wave boundary.

Fig. 4(a) shows hull-mass velocity histories computed with spectral elements of four different orders, along with the corresponding benchmark (24,001-DOF CAFE) history. All of the spectral-element models possess 81 DOF, and the $N = 1$ CASE model constitutes a CAFE model. The C-values appearing in the legend are the values of comprehensive error for the various CASE-calculated histories, as referenced to the benchmark history. We observe that comprehensive error steadily decreases with increasing element order for the fixed number of DOF. We also observe the spurious oscillations due to frothing for $N = 4$, 8, and 16.

Also shown in Fig. 4(a) is the benchmark history produced when cavitation is precluded (acoustic fluid). We see that cavitation profoundly affects structural response.

Fig. 4(b) shows the space–time "cavitation zones" that correspond to the benchmark response of Fig. 4(a). The gray areas indicate the existence of cavitation, where and when absolute pressure is zero. It is seen that cavitation closures at $t = 49$ ms, $X = 1.23$ m, and at $t = 129$ ms, $X = 0.08$ m, produce the near discontinuities in the velocity histories at times that reflect propagation of the closure disturbances at the speed of sound.

One might very well accept the $N = 1$ (CAFE) calculation in Fig. 4(a), characterized by $C \approx 0.1$, as satisfactory. However, a corresponding three-dimensional calculation would involve roughly $81^3 > 500{,}000$ DOF. Hence, we seek $C \approx 0.1$ accuracy with many fewer than 81 DOF in the one-dimensional calculation. Fig. 5 shows C-values plotted versus DOF values for the spectral elements of four different orders and several element sizes. Although the $N = 4$ element shows little improvement over the CAFE element, the $N = 8$ and $N = 16$ elements provide considerable gains. For example, about 90 CAFE DOF are required to achieve $C = 0.1$ accuracy, but only about 40 $N = 8$ CASE DOF are required to do so. In a corresponding three-dimensional calculation, this amounts to an order-of-magnitude reduction.

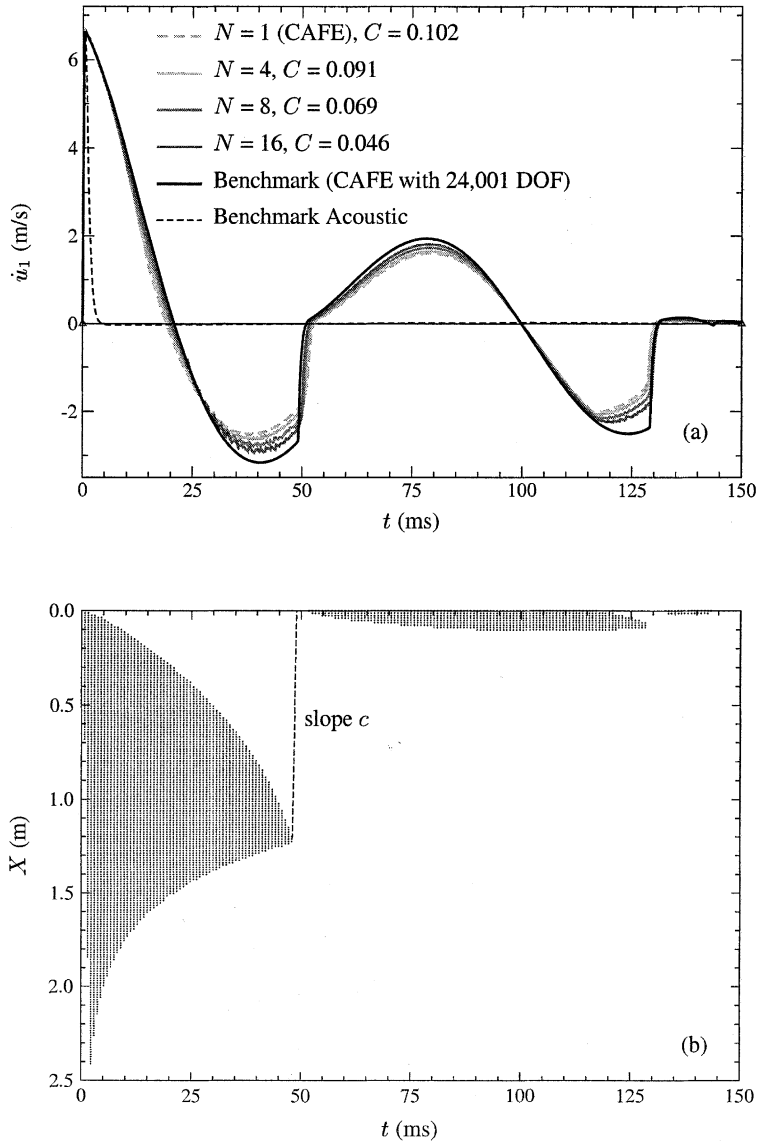

Fig. 4. (a) Hull-mass response histories calculated with four 81-DOF CASE models ($d_{PW} = 3$ m); C-values are the comprehensive error factors for the CASE-calculated histories relative to the benchmark history. (b) The cavitation zones pertain to the benchmark CAFE model.

In practice, it is more likely that a modeler using CASE will choose a "base" mesh and refine with higher-order polynomials (p refinement). In contrast, a CAFE modeler will refine the fluid mesh by employing more, but smaller, elements (h refinement). Here, we use a base fluid model with 0.3 m elements and refine by either (i) reducing the size of the elements while keeping $N = 1$ (CAFE refinement) or (ii) increasing the polynomial order of the elements (CASE refinement). Fig. 6 shows C-values plotted versus DOF for CAFE and CASE refinement. Although CASE refinement requires only 38% fewer DOF than CAFE refinement to reach a comprehensive error of 0.1, it offers much better convergence at lower error levels.

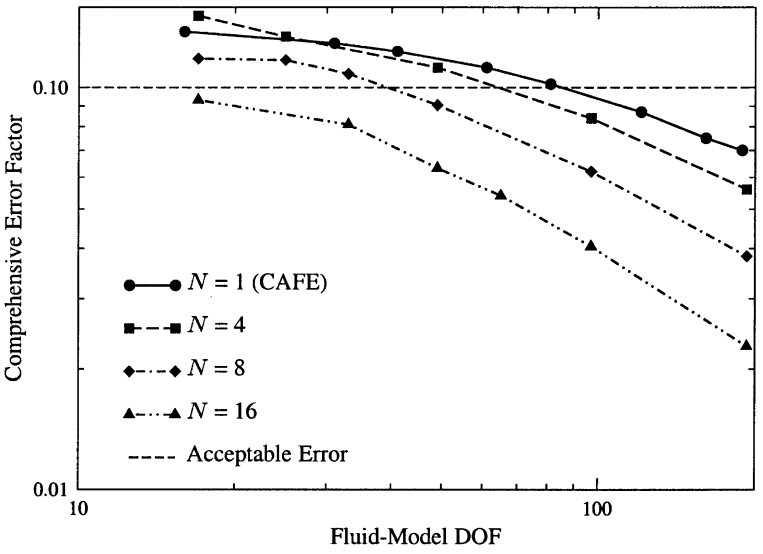

Fig. 5. Comprehensive error factors as a function of fluid-model DOF pertaining to $\dot{u}_1$ histories for CASE models with several element sizes ($d_{PW} = 3$ m, $0 \leqslant t \leqslant 150$ ms).

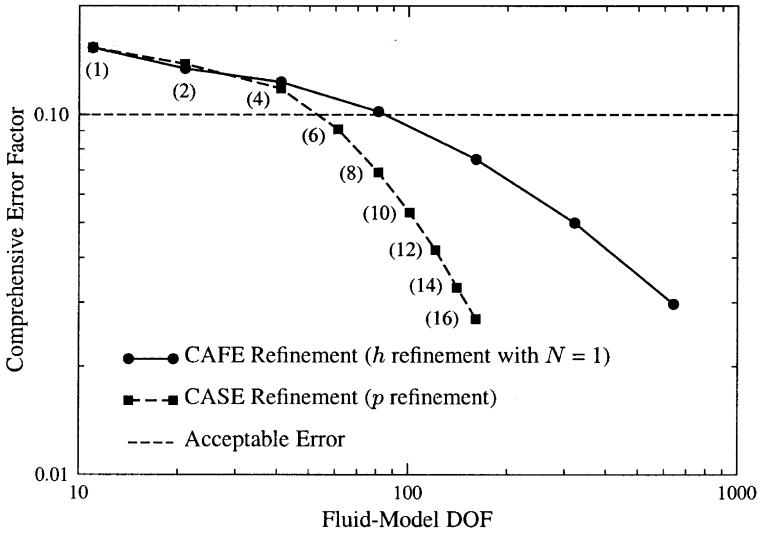

Fig. 6. Comprehensive error factors as a function of fluid-model DOF pertaining to $\dot{u}_1$ histories for either CAFE or CASE refinement of a base fluid model with 0.3 m elements ($d_{PW} = 3$ m, $0 \leqslant t \leqslant 150$ ms). The numbers in parentheses indicate the values of N for CASE refinement.

A disadvantage of the CASE method is the increased bandwidth of the reactance matrix **H** caused by increased nodal coupling within an element. Further, for a given number of fluid DOF, CASE requires more time steps due to the smaller CFL increment limit. To investigate these issues, we examine Figs. 7 and 8, which show C-values versus total fluid-model operation counts for the calculations behind Figs. 5 and 6, respectively. To achieve $C = 0.1$ accuracy with h refinement, the $N = 4$ CASE element requires 10% more,

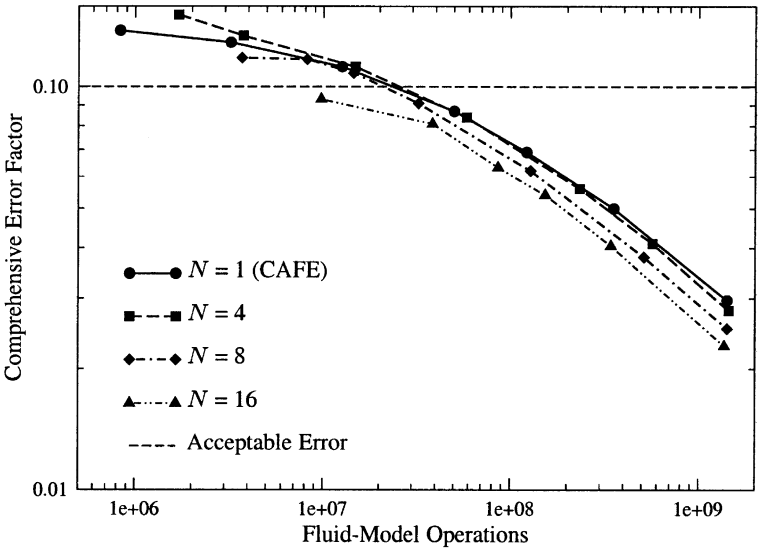

Fig. 7. Comprehensive error factors as a function of fluid-model operations pertaining to $\dot{u}_1$ histories for CASE models with several element sizes ($d_{PW} = 3$ m, $0 \leqslant t \leqslant 150$ ms).

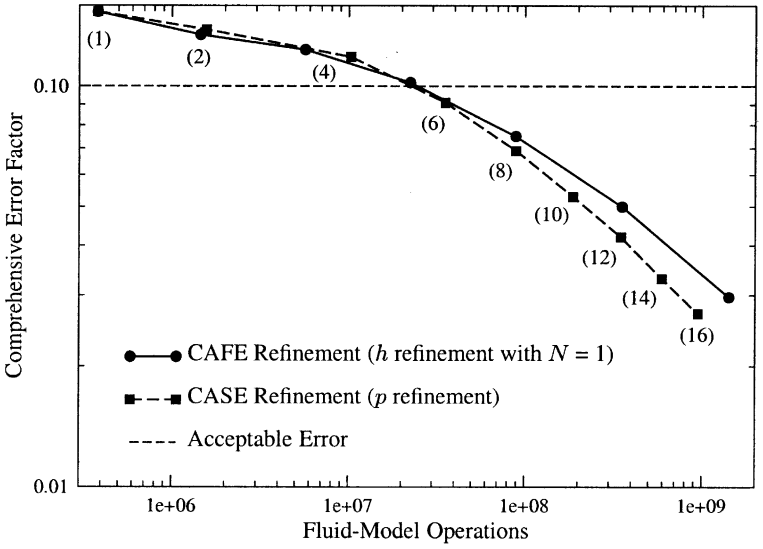

Fig. 8. Comprehensive error factors as a function of total fluid-model operations pertaining to $\dot{u}_1$ histories produced with either CAFE or CASE refinement of a base fluid model with 0.3 m elements ($d_{PW} = 3$ m, $0 \leqslant t \leqslant 150$ ms). The numbers in parentheses indicate the values of N for CASE refinement.

the $N = 8$ CASE element requires 25% fewer, and the $N = 16$ CASE element requires (with $C = 0.093$) 68% fewer operations than does the CAFE element. In Fig. 8, CAFE and CASE require approximately the same number of operations to achieve $C = 0.1$. However, for greater accuracy, CASE refinement requires fewer operations than CAFE refinement. Hence, for a given level of accuracy, the decrease in the required fluid

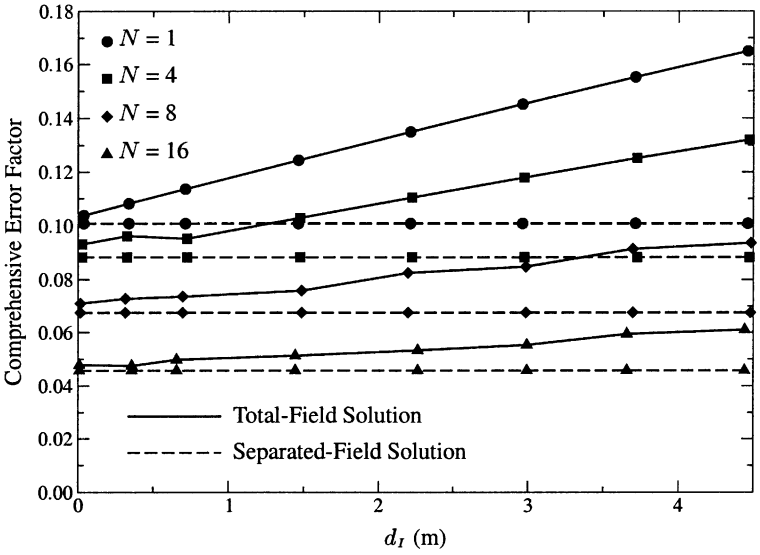

Fig. 9. Comprehensive error factors pertaining to CASE-calculated $\dot{u}_1$ histories for various standoffs with and without field separation ($d_{PW} = 6$ m, 161 DOF, $0 \leqslant (t - d_1/c) \leqslant 150$ ms).

DOF for CASE offsets the penalties associated with the increased operation counts due to smaller CFL limits and larger **H** bandwidths.

4.2. Evaluation of field separation

For this evaluation, one-dimensional CASE calculations are initiated with the incident wavefront located at various standoffs from the wet surface of the hull mass. To capture the peak of the step-exponential wavefront in the separated-field solution, the wavefront location at $t = 0$ was shifted slightly ($<c\Delta t$) so that the incident-wave peak contacted the structure exactly at the beginning of a time increment.

The CASE models all contain 161 DOF, with the plane-wave boundary placed at $d_{PW} = 6$ m. The calculations fall into two groups, the first pertaining to the total-field formulation (2) and the second to the separated-field formulation (13).

Fig. 9 shows C-values for the hull-mass velocity histories produced by the four models plotted against standoff values. We observe that, for all elements, total-field solution error increases almost monotonically with standoff, whereas separated-field solution error remains unchanged. We also observe that the average rate of C-value increase decreases with increasing N. This, of course, is due to the low-dispersion attribute of spectral elements.

Finally, Fig. 10 shows pressure-field snapshots of the incident wave generated by the four CASE models for $d_I = 4.5$ m. The differences between the exact snapshots and the CASE-calculated snapshots expose significant numerical dispersion in the latter. The dispersion clearly decreases with increasing element order.

5. Conclusion

We have demonstrated that the accuracy of finite-element simulations of the transient response of an acoustic fluid subject to cavitation may be considerably improved by employing high-order spectral elements. Additional accuracy may be achieved by separating the total field into equilibrium, incident, and

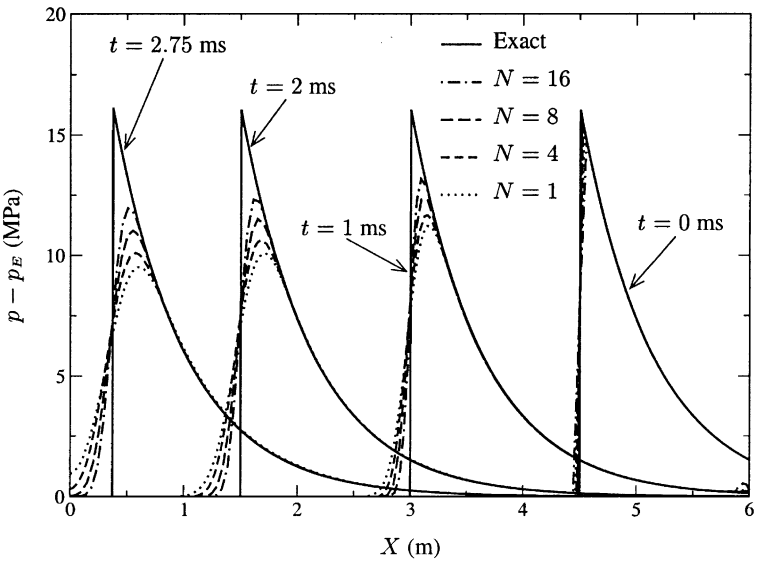

Fig. 10. Incident-wave pressure snapshots, exact separated-field and as calculated with four total-field CASE models ($d_{PW} = 6$ m, $d_I = 4.5$ m, 161 DOF).

scattered fields, where the first and second are much easier to determine than the third. The impact of these improvements in underwater-shock analysis is to admit the possibility of practical three-dimensional engineering computations.

Acknowledgements

This research was funded by the Office of Naval Research under Grant N00014-01-1-0154. The authors express their appreciation to Dr. Luise Couchman and Mr. Stephen Schreppler of ONR and to Mr. Michael Riley of NSWCCD for their interest and support.

References

[1] H.H. Bleich, I.S. Sandler, Interaction between structures and bilinear fluids, International Journal of Solids and Structures 6 (1970) 617–639.
[2] S.K. Chan, A modified finite element procedure for underwater shock analysis, in: Proceedings of the 61st Shock and Vibration Symposium, San Diego, CA, 3, 1990, pp. 87–101.
[3] S.K. Chan, An improvement in the modified finite element procedure for underwater shock analysis, in: Proceedings of the 63rd Shock and Vibration Symposium, SAVIAC, Arlington, VA, 1992, pp. 616–627.
[4] R.D. Cook, D.S. Malkus, M.E. Plesha, Concepts and Applications of Finite Element Analysis, Wiley, New York, 1989.
[5] W. Dauksher, A.F. Emery, Accuracy in modeling the acoustic wave equation with Chebyshev spectral finite elements, Finite Elements in Analysis and Design 26 (1997) 115–128.
[6] M.R. Driels, The effect of a non-zero cavitation tension on the damage sustained by a target plate subject to an underwater explosion, Journal of Sound and Vibration 73 (4) (1980) 533–545.
[7] C.A. Felippa, J.A. DeRuntz, Finite element analysis of shock-induced hull cavitation, Computer Methods in Applied Mechanics and Engineering 44 (1984) 297–337.
[8] C.A. Felippa, J.A. DeRuntz, Acoustic fluid volume modeling by the displacement potential formulation with emphasis on the wedge element, Computers and Structures 41 (4) (1991) 669–686.

[9] P.F. Fischer, Analysis and application of a parallel spectral element method for the solution of the Navier–Stokes equations, Computer Methods in Applied Mechanics and Engineering 80 (1990) 483–491.
[10] T.L. Geers, An objective error measure for the comparison of calculated and measured transient response histories, The Shock and Vibration Bulletin 54 (1984) 99–107.
[11] E.H. Kennard, Cavitation in an elastic liquid, Physical Review 63 (5/6) (1943) 172–181.
[12] D. Komatitsch, J.P. Vilotte, The spectral element method: An efficient tool to simulate the seismic response of 2D and 3D geological structures, Bulletin of the Seismological Society of America 88 (2) (1998) 368–392.
[13] Y. Maday, A.T. Patera, Spectral element methods for the incompressible Navier–Stokes equations, in: A.K. Noor, J.T. Oden (Eds.), State-of-the-Art Surveys on Computational Mechanics, The American Society of Mechanical Engineers, New York, 1989, pp. 71–142.
[14] K.J. Marfurt, Accuracy of finite-difference and finite-element modeling of the scalar and elastic wave equations, Geophysics 49 (5) (1984) 533–549.
[15] P.M. Morse, H. Feshbach, Methods of Theoretical Physics, McGraw-Hill, New York, 1953.
[16] W.A. Mulder, Spurious modes in finite-element discretizations of the wave equation may not be all that bad, Applied Numerical Mathematics 30 (1999) 425–445.
[17] R.E. Newton, Effects of cavitation on underwater shock loading– axisymmetric geometry, Technical Report NPS-69-78-017PR, Naval Postgraduate School, Monterey, CA, 1978.
[18] R.E. Newton, Effects of cavitation on underwater shock loading—part 1, Technical Report NPS-69-78-013, Naval Postgraduate School, Monterey, CA, 1978.
[19] R.E. Newton, Finite element analysis of shock-induced cavitation, 1980, Preprint 80-110, ASCE Spring Convention.
[20] R.E. Newton, Effects of cavitation on underwater shock loading—plane problem, Technical Report NPS-69-81-001, Naval Postgraduate School, Monterey, CA, 1981.
[21] A.T. Patera, A spectral element method for fluid dynamics: laminar flow in a channel expansion, Journal of Computational Physics 54 (1984) 468–488.
[22] E. Priolo, J.M. Carcione, G. Seriani, Numerical simulation of interface waves by high-order spectral modeling techniques, Journal of the Acoustical Society of America 95 (2) (1994) 681–693.
[23] E.M. Ronquist, A.T. Patera, A Legendre spectral element method for the Stefan problem, International Journal for Numerical Methods in Engineering 24 (1987) 2273–2299.
[24] G. Seriani, E. Priolo, Spectral element method for acoustic wave simulation in heterogeneous media, Finite Elements in Analysis and Design 16 (1994) 337–348.
[25] Y.S. Shin, L.D. Santiago, Surface ship shock modeling and simulation: two-dimensional analysis, Shock and Vibration 5 (1998) 129–137.
[26] M.A. Sprague, Advances in computational methods for fluid–structure-interaction problems, Master's thesis, University of Colorado at Boulder, 1999.
[27] M.A. Sprague, T.L. Geers, Response of empty and fluid-filled, submerged spherical shells to plane and spherical, step-exponential acoustic waves, Shock and Vibration 6 (1999) 147–157.
[28] M.A. Sprague, T.L. Geers, Computational treatment of cavitation effects in near-free-surface underwater shock analysis, Shock and Vibration 8 (2) (2001) 105–122.
[29] M.M. Swisdak, (Ed.), Explosion Effects and Properties: Part II—Explosion Effects in Water, NSWC/WOL TR 76-116. NSWC, Feb 1978.
[30] A. Taflove, S.C. Hagness, Computational Electrodynamics: The Finite-Difference Time-Domain Method, Artech House, Boston, 2000.
[31] J.E. van Aanhold, G.J. Meijer, P.P.M. Lemmen, Underwater shock response analysis of a floating vessel, Shock and Vibration 5 (1998) 53–59.
[32] O.C. Zienkiewicz, R.L. Taylor, The Finite Element Method, McGraw-Hill, London, 1994.